Fast and Unconditional All-Microwave Reset of a Superconducting Qubit

P. Magnard,[1,*] P. Kurpiers,[1] B. Royer,[2] T. Walter,[1] J.-C. Besse,[1] S. Gasparinetti,[1]
M. Pechal,[1] J. Heinsoo,[1] S. Storz,[1] A. Blais,[2,3] and A. Wallraff[1]

[1]*Department of Physics, ETH Zürich, CH-8093 Zürich, Switzerland*
[2]*Institut Quantique and Département de Physique, Université de Sherbrooke,
Sherbrooke, Québec J1K 2R1, Canada*
[3]*Canadian Institute for Advanced Research, Toronto, Ontario M5G IZ8, Canada*

Active qubit reset is a key operation in many quantum algorithms, and particularly in quantum error correction. Here, we experimentally demonstrate a reset scheme for a three-level transmon artificial atom coupled to a large bandwidth resonator. The reset protocol uses a microwave-induced interaction between the $|f, 0\rangle$ and $|g, 1\rangle$ states of the coupled transmon-resonator system, with $|g\rangle$ and $|f\rangle$ denoting the ground and second excited states of the transmon, and $|0\rangle$ and $|1\rangle$ the photon Fock states of the resonator. We characterize the reset process and demonstrate reinitialization of the transmon-resonator system to its ground state in less than 500 ns and with 0.2% residual excitation. Our protocol is of practical interest as it has no additional architectural requirements beyond those needed for fast and efficient single-shot readout of transmons, and does not require feedback.

The efficient initialization of a set of qubits into their ground state is one of the DiVincenzo criteria for quantum information processing [1]. Initialization is also critical for the implementation of error correction codes [2–4] to reset ancilla qubits on demand to a fiducial state in short time and with high fidelity. For this reason, qubit reset procedures have been implemented for a wide range of physical quantum computation platforms [5–9], including superconducting qubits for which we discuss the most common approaches below [10–19].

Reset for superconducting qubits is commonly realized using the outcome of a strong projective measurement to either herald the ground state [13] or deterministically prepare it using feedback [14–17]. Measurement-induced state mixing limits the achievable single-shot readout fidelity and the performance of this approach [16,20,21]. In addition, measurement-induced mixing constrains the quantum-nondemolition nature of dispersive readout giving rise to leakage out of the qubit subspace [16,22], which is particularly detrimental to quantum error correction [23].

Alternatively, qubit reset can be achieved by coupling the qubit excited state to a cold and rapidly decaying quantum system. Such driven reset schemes [10,11,18,24,25] make use of ideas related to dissipation engineering [26–29]. In one variant of this approach [11], the qubit is quickly tuned into resonance with a Purcell filtered, large-bandwidth, resonator using magnetic flux. The qubit then quickly thermalizes to its ground state due to Purcell decay, the rate of which can be adjusted, on-demand, by 3 orders of magnitude. The flux pulses employed in this scheme require careful calibration, they may affect subsequent

gates by bleedthrough and neighboring qubits through cross talk [30].

An all-microwave reset protocol utilizing the qubit-state-dependent response of a resonator [18] avoids the use of flux tuning and its potentially detrimental effects. This protocol [18] has minimal hardware requirements, only a single resonator, but requires a cavity linewidth κ smaller than the dispersive interaction strength χ limiting both the speed of the reset process and the readout if the same resonator is used [31,32].

In this work, we demonstrate an alternative all-microwave reset protocol of a three-level transmon coupled to a resonator with no constraint on κ. Driving the transmon simultaneously with two coherent tones forms a Λ system in the Jaynes-Cumming ladder [33] and unconditionally transfers any excitation in the two lowest excited states of the transmon to a single photon emitted to the environment, thus resetting the transmon qutrit on demand. This protocol outperforms existing measurement-based and all-microwave driven reset schemes in speed and fidelity [34], populates the resonator with one photon at most, and can be extended to other types of superconducting qubits. In addition, this protocol is of practical interest as it is optimized when the resonator is designed for rapid and high-fidelity transmon readout [32].

The device used in our experiment and schematically illustrated in Fig. 1(a), uses a transmon qubit [35,36] (orange), with transition frequency $\omega_{ge}/2\pi = 6.343$ GHz, anharmonicity $\alpha/2\pi = -265$ MHz and energy relaxation time $T_1 = 5.5$ μs. We control the qubit state with microwave pulses up-converted from an arbitrary waveform

generator (AWG), applied to the transmon through a dedicated drive line. To perform the reset, the transmon is capacitively coupled with rate $g_r/2\pi = 335$ MHz to a resonator of frequency $\omega_r/2\pi = 8.400$ GHz, resulting in a dispersive interaction with rate $\chi_r/2\pi = -6.3$ MHz (light blue). The reset resonator is connected through a Purcell-filter resonator to cold 50 Ω loads with an effective coupling $\kappa/2\pi = 9$ MHz. This resonator can, in principle, be used for transmon readout. However, in the present work, to decouple the reset from its characterization process, we read out the transmon with a dedicated, Purcell-filtered resonator (light green). We present further details about the sample in the Supplemental Material [34].

We read out the transmon state using a gated drive applied to the input port of the readout resonator at a frequency optimized for qutrit readout [37]. The signal scattered off the readout resonator is amplified at $T_{BT} = 10$ mK by a Josephson parametric amplifier [38,39]. The signal is then amplified at 4 K with high electron mobility transistors, down-converted using an I-Q mixer, digitized using an analog-to-digital converter, digitally down-converted and processed using a field programmable gate array.

The reset concept, illustrated in Fig. 1(b), is based on a cavity-assisted Raman transition between $|f,0\rangle$ and $|g,1\rangle$ [33,40,41]. Here, $|s,n\rangle$ denotes the tensor product of the transmon in state $|s\rangle$, with its three lowest energy eigenstates $|g\rangle$, $|e\rangle$, and $|f\rangle$, and the reset resonator in the n photon Fock state $|n\rangle$. By simultaneously driving the $|f,0\rangle \leftrightarrow |g,1\rangle$ ($f0$-$g1$) transition and the $|e,0\rangle \leftrightarrow |f,0\rangle$ (e-f) transition, the population is transferred from the qutrit excited states, $|e,0\rangle$ and $|f,0\rangle$, to the state $|g,1\rangle$. The system then rapidly decays to the target dark state $|g,0\rangle$ by photon emission at rate κ, effectively resetting the qutrit to its ground state.

We model the dynamics of the reset by the non-Hermitian Hamiltonian

$$H/\hbar = \begin{bmatrix} -\delta_{ef} & \Omega_{ef} & 0 \\ \Omega_{ef}^* & 0 & \tilde{g} \\ 0 & \tilde{g}^* & -\delta_{f0g1} - i\kappa/2 \end{bmatrix}, \quad (1)$$

acting on the states $|e,0\rangle$, $|f,0\rangle$, and $|g,1\rangle$. Here, the non-Hermitian term $-i\kappa/2$ accounts for the photon emission process, and Ω_{ef} and $\tilde{g}$ are the e-f and $f0$-$g1$ drive-induced Rabi rates, respectively. Because the $f0$-$g1$ drive acts on a second order transition, it requires a high amplitude V_{f0g1} and induces significant ac Stark shifts $\bar{\Delta}_{ef}$ and $\bar{\Delta}_{f0g1}$ of the e-f and $f0$-$g1$ transitions [40]. In Hamiltonian (1), δ_{ef} and δ_{f0g1} denote the detuning of the drives from their respective ac Stark shifted transitions. Therefore, gaining experimental control over the reset drive parameters requires us to characterize the dependence of $\bar{\Delta}_{ef}$ and $\bar{\Delta}_{f0g1}$ on V_{f0g1} as well as the relation between the drive amplitudes and their corresponding Rabi rates.
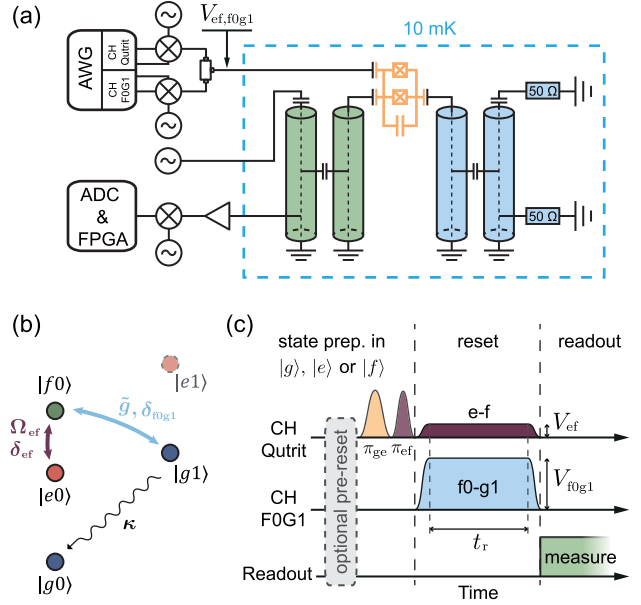

FIG. 1. (a) Simplified schematic of the experimental setup. A transmon (orange) is coupled to two Purcell-filtered resonators. The readout resonator (green) is connected to room temperature electronics (description in the main text), while the reset resonator (blue) is connected to two 50 Ω loads thermalized at base temperature. (b) Jaynes-Cummings ladder diagram of the transmon-reset resonator energy levels. The purple and light blue arrows represent the e-f and $f0$-$g1$ pulsed coherent drives, respectively, and the black arrow labeled κ illustrates the resonator decay process. (c) Illustration of the pulse schemes used to test the reset protocol. We initialize the qutrit to its ground state passively or optionally with an unconditional reset, then prepare the desired state $|g\rangle$, $|e\rangle$, or $|f\rangle$ with control pulses (labeled π_{ge} and π_{ef}). We reset the qutrit by simultaneously applying flattop e-f (purple) and $f0$-$g1$ (light blue) pulses for a reset time t_r. The resulting qutrit state is then measured by applying a microwave tone to the readout resonator (green).

First, we determine the ac Stark shift $\bar{\Delta}_{f0g1}$. We initialize the transmon in $|g\rangle$, then apply a sequence of two π pulses (π_{ge}, π_{ef}) to prepare the system in $|f,0\rangle$ [Fig. 1(c)]. We apply a flattop $f0$-$g1$ pulse of carrier frequency ν_{f0g1}, amplitude V_{f0g1} and duration t_r and read out the resulting transmon state populations. Here and in all calibration measurements, the populations $P_{g,e,f}$ of the transmon qutrit are extracted by comparing the averaged signal transmitted through the readout resonator to reference traces [37]. We repeat the process varying ν_{f0g1} and V_{f0g1}, while keeping $V_{f0g1}t_r$ fixed to obtain comparable Rabi angles for the rotations induced by the $f0$-$g1$ drive. For a given value of V_{f0g1}, we fit the dependence of P_g on ν_{f0g1} to a Gaussian whose center yields the ac Stark shifted frequency, at which the population transfer from $|f,0\rangle$ to $|g,1\rangle$ is maximized [Fig. 2(a)]. The ac Stark shift $\bar{\Delta}_{f0g1}$ extracted in this way shows a quadratic dependence on V_{f0g1} [blue diamonds in Fig. 2(b)].
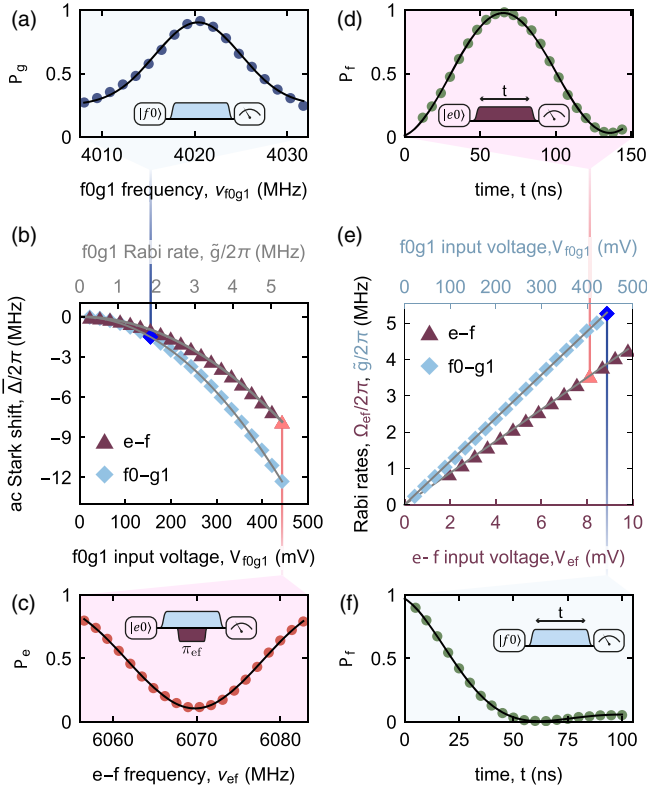
FIG. 2. (a) Population P_g vs the frequency ν_{f0g1} of a flattop $f0$-$g1$ pulse, of amplitude V_{f0g1}, applied to the qutrit initially prepared in $|f, 0\rangle$. (b) Measured ac Stark shifts $\bar{\Delta}_{f0g1}$ and $\bar{\Delta}_{ef}$ of the $f0$-$g1$ (blue diamonds) and e-f (purple triangles) transitions, vs amplitude V_{f0g1} of the f0-g1 drive. The solid lines are quadratic fits to the data. (c) Population P_e vs frequency ν_{ef} of a flattop e-f π pulse applied on the qutrit, initially prepared in state $|e, 0\rangle$, in the presence of a continuous $f0$-$g1$ drive of amplitude V_{f0g1}. (d) Population P_f vs duration t of a resonant flattop e-f pulse, of amplitude $V_{ef} = 8$ mV. (e) Extracted Rabi rates Ω_{ef} and $\tilde{g}$, of the e-f (purple triangles) and $f0$-$g1$ (blue diamonds) drives versus their amplitude, V_{ef} and V_{f0g1}. The solid lines are linear fits. (f) Population P_f vs duration t of a resonant square $f0$-$g1$ pulse, of amplitude $V_{f0g1} = 444$ mV. The pulse schemes used to acquire the data shown in panels (a), (c), (d), and (f) are shown as insets, with the $f0$-$g1$ and e-f pulse envelopes represented in blue and purple, respectively. The solid lines in (a) and (c) are fits to Gaussians. The solid lines in (c) and (f) are fits to Rabi oscillation models described in Ref. [34].

To determine $\bar{\Delta}_{ef}$, we prepare the system in $|e, 0\rangle$ and apply a short square e-f π pulse of frequency ν_{ef} in the presence of a continuous, resonant f0-g1 drive of amplitude V_{f0g1}. For each V_{f0g1}, we extract the ac Stark shifted frequency of the e-f transition by finding the minimum of P_e vs ν_{ef} with a fit to a Gaussian [Fig. 2(c)]. As before, we observe a quadratic dependence of $\bar{\Delta}_{ef}$ on V_{f0g1} [purple triangles in Fig. 2(b)].

Finally, we perform resonant Rabi oscillation measurements on the e-f and $f0$-$g1$ transitions to extract the linear

relation between the drive amplitudes V_{ef} and V_{f0g1}, and their corresponding Rabi rates [34] [Figs. 2(d)–2(f)]. The Rabi oscillations between $|f, 0\rangle$ and $|g, 1\rangle$ are damped due to the spontaneous decay from $|g, 1\rangle$ to $|g, 0\rangle$ [Fig. 2(f)].

In all the following experiments, we adjust the drive frequencies such that $\delta_{ef} = \delta_{f0g1} = 0$ to reset the transmon, leaving only $\tilde{g}$ and Ω_{ef} as tunable parameters. From Eq. (1), we derive the time dependence of the population

$$P_{s|s_0}^H(t) = \left| \sum_k \langle s|\hat{A}_k|s_0\rangle e^{-i\lambda_k t} \right|^2 \qquad (2)$$

of state $|s\rangle \in \{|e, 0\rangle, |f, 0\rangle, |g, 1\rangle\}$ during the reset. Here, $|s_0\rangle$ is the initial state of the system, λ_k are the eigenvalues of Hamiltonian (1) and $\hat{A}_k$ are operators that depend only on Hamiltonian (1) [34]. These populations oscillate at rates $2\text{Re}(\lambda_k)$ and decay exponentially at rates $2|\text{Im}(\lambda_k)|$. As the smallest decay rate dominates at long reset times, we define the reset rate as $\Gamma \equiv \min[2|\text{Im}(\lambda_k)|]$. The reset can be operated in two regimes [34]. In the low drive-power region hatched in Fig. 3(a), the eigenvalues λ_k are purely imaginary: the reset is in an overdamped regime where the qutrit excited populations decay with no oscillation. When crossing the critical damping boundary, two eigenvalues abruptly display a finite real part and the reset enters an underdamped, oscillatory regime. The reset rate Γ is bounded by its maximum value $\kappa/3$, which it reaches on a line in parameter space, defining an optimal branch (solid red line in Fig. 3). The optimal branch intersects the critical-damping boundary at an exceptional point (black cross in Fig. 3) where all three eigenvalues are identical [42]. At this point, the reset has maximum rate and displays no oscillations. For a given $\tilde{g}$, there is a unique value of Ω_{ef} maximizing the reset rate to $\Gamma_{\max}(\tilde{g})$. The parameter configuration then lies on the critical-damping boundary if $\tilde{g}$ is below its value at the exceptional point
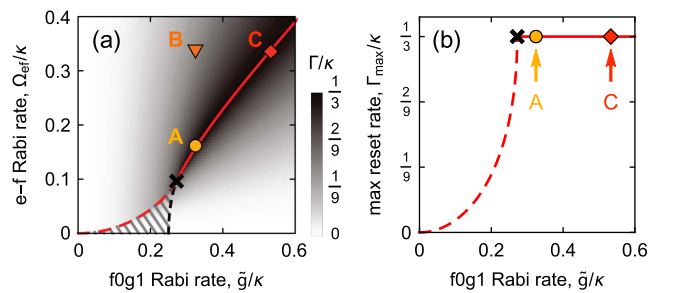

FIG. 3. (a) Calculated reset rate Γ/κ, vs Rabi rates $\tilde{g}/\kappa$ and Ω_{ef}/κ. The overdamped parameter region is hatched. The red line shows the values of Ω_{ef} maximizing Γ as a function of $\tilde{g}$, and corresponds to the optimal branch where it is solid. (b) Maximized reset rate $\Gamma_{\max}/\kappa$ vs $\tilde{g}/\kappa$ [we follow the red line from (a)]. In (a) and (b), the parameter configurations A, B, and C at which the reset dynamic was probed (see main text and Fig. 4) are indicated with colored symbols and the exceptional point is represented by a black cross.

$\tilde{g}_{\rm ep} = \sqrt{2/27}\kappa$ (red dashed line in Fig. 3), and on the optimal branch otherwise. As $\tilde{g}$ goes below $\tilde{g}_{\rm ep}$, $\Gamma_{\max}(\tilde{g})$ abruptly drops [Fig. 3(b)]. Therefore, the ability to drive the $f0$-$g1$ transition with $\tilde{g} > \tilde{g}_{\rm ep}$ is crucial to achieve fast reset.

We probed the reset dynamics at the three parameter configurations labeled A, B, and C in Fig. 3(a). We initialize the transmon in $|e, 0\rangle$ or $|f, 0\rangle$, apply the reset drive pulses for a time t_r, and then readout the transmon with single-shot measurements, as illustrated in Fig. 1(c). Utilizing the single-shot statistics, we correct for the qutrit state assignment errors, to determine the population of the qutrit with systematic errors below 0.3% [34]. We first probed the reset in configuration A ($\Omega_{ef}/2\pi = 1.5$ MHz, $\tilde{g}/2\pi = 2.9$ MHz), which is on the optimal branch and is the closest to the exceptional point. During the reset, the transmon state oscillates between $|g\rangle$, $|e\rangle$, and $|f\rangle$ while rapidly decaying to $|g\rangle$ on a timescale of 300 ns, independent of the initial state [Figs. 4(a) and 4(b)]. The excited population $P_{\rm exc} = P_e + P_f$ drops to below 1% without displaying any oscillations [Fig. 4(c)]. The reset dynamics calculated from Eq. (2) is in excellent agreement with the data, as shown by the solid lines in Figs. 4(a) and 4(b). When increasing the e-f drive to $\Omega_{ef}/2\pi = 3$ MHz (B), the decaying state $|g, 1\rangle$ is populated earlier. As a result, we observe that $P_{\rm exc}$ drops faster initially but at a slower rate at longer times since configuration B is not on the optimal branch [Fig. 4(c)]. Because this parameter set realizes the underdamped regime, $P_{\rm exc}$ displays oscillatory features. Configuration C ($\Omega_{ef}/2\pi = 3$ MHz, $\tilde{g}/2\pi = 4.8$ MHz) is on the optimal branch and has higher drive rates than configuration A. Therefore, $P_{\rm exc}$ drops faster initially, and with the same long-time rate, leading to a more efficient reset. In this configuration, $P_{\rm exc}$ drops below 1% in only 280 ns, and below measurement errors (~0.3%) in steady state [Fig. 4(c)], outperforming all existing measurement-based and microwave-driven reset schemes by an order of magnitude [34].

At long reset times, $P_{\rm exc}$ saturates to a nonzero steady-state value $P_{\rm exc}^{\rm sat}$ because of transmon rethermalization. To fully capture the role of decoherence and rethermalization during the reset, we perform master equation simulations using only parameters extracted from independent measurements [34]. The numerical simulations are in excellent agreement with the data for all probed reset parameter configurations [solid lines in Fig. 4(c)] and yield $P_{\rm exc}^{\rm sat} = 0.2\%$ for configuration C, suggesting that the $P_{\rm exc}^{\rm sat}$ achievable in our experiment is limited by transmon rethermalization. In this case, the excited population saturates at $P_{\rm exc}^{\rm sat} = k_\uparrow \tau$, where $k_\uparrow \simeq n_{\rm th}/T_1$ is the rethermalization rate, with $n_{\rm th}$ the excited population at thermal equilibrium, and $\tau = \int_0^\infty [P_{e|e}^H + P_{f|e}^H](t)dt$ [34]. Therefore, faster drops of $P_{\rm exc}$, obtained by increasing the drive rates along the optimal branch, result in lower steady-state excited populations [Fig. 4(c)]. Other limitations, such as residual driving of the g-e transition by the e-f drive, and finite temperature of the resonator, are negligible for the presented parameters [34].

High transmon anharmonicity α combined with large transmon-resonator coupling g allows for reaching larger Ω_{ef} and $\tilde{g}$ without driving unwanted transitions [40]. Driving the reset at higher Rabi rates, we can reach the optimal branch, where $\Gamma = \kappa/3$, for larger values of κ. As a result, increasing g, α, and κ maximizes Γ and optimizes the reset. Increasing these parameters also optimizes speed and fidelity of qubit readout without degrading the coherence and thermalization of the qubit, if Purcell filters are used [32,34]. Therefore, our reset protocol performs best with a resonator designed for optimal readout. As an illustration, using the results of the present work, we calculate that implementing this reset protocol with the readout resonator of Ref. [32] would reset the qutrit below $P_{\rm exc} = 0.1\%$ in 83 ns, and to a steady-state value $P_{\rm exc}^{\rm sat} = 1.6 \times 10^{-4}$ in 200 ns, provided that the $f0$-$g1$ Rabi rate exceeds $\sqrt{2/27}\kappa \simeq 2\pi \times 10$ MHz.

In conclusion, we have demonstrated an unconditional all-microwave protocol to reset the state of a three-level transmon below 1% excitation in less than 280 ns. This reset
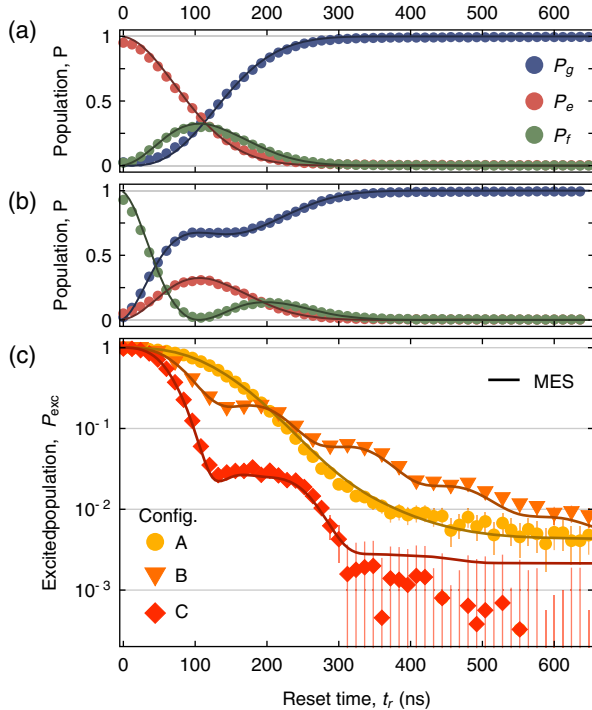

FIG. 4. Qutrit populations $P_{g,e,f}$ vs reset time t_r with reset parameters in configuration A (see main text), and (a) system initialized in $|e, 0\rangle$ or (b) in $|f, 0\rangle$. The solid lines in (a) and (b) are calculated from Eq. (2). (c) Excited population $P_{\rm exc}$ as a function of reset time t_r, when the qutrit is initialized in $|e, 0\rangle$, shown for reset parameter configurations A, B, and C. The solid lines are calculated from a master equation simulation.

scheme does neither require feedback, nor qubit tunability, not does it constrain device parameters or populate the readout resonator with a large number of photons. Furthermore, the protocol can conveniently be integrated in an architecture where the qubits are coupled to high bandwidth, Purcell-filtered resonators, in order to perform rapid and high-fidelity quantum manipulations [43] and readout [32,44]. However, in a multiqubit system, the protocol's need for high $f0$-$g1$ drive power increases the sensitivity to cross talk and can cause spurious driving of two-qubit transitions. Addressing these concerns in scaled up circuits will require improved shielding of drive lines, and careful selection of resonator and qubit frequencies. We did not observe any degradation of qubit coherence and operation fidelity in the presence of the reset drive tones [43], but a systematic study of these effects constitutes valuable future work.

---

*Corresponding author.
pmagnard@phys.ethz.ch

[1] D. P. DiVincenzo, Fortschr. Phys. **48**, 771 (2000).

[2] P. Schindler, J. T. Barreiro, T. Monz, V. Nebendahl, D. Nigg, M. Chwalla, M. Hennrich, and R. Blatt, Science **332**, 1059 (2011).

[3] M. D. Reed, L. DiCarlo, S. E. Nigg, L. Sun, L. Frunzio, S. M. Girvin, and R. J. Schoelkopf, Nature (London) **482**, 382 (2012).

[4] J. Chiaverini, D. Leibfried, T. Schaetz, M. Barrett, R. Blakestad, J. Britton, W. Itano, J. Jost, E. Knill, C. Langer, R. Ozeri, and D. Wineland, Nature (London) **432**, 602 (2004).

[5] C. Monroe, D. M. Meekhof, B. E. King, S. R. Jefferts, W. M. Itano, D. J. Wineland, and P. Gould, Phys. Rev. Lett. **75**, 4011 (1995).

[6] F. Jelezko, T. Gaebel, I. Popa, A. Gruber, and J. Wrachtrup, Phys. Rev. Lett. **92**, 076401 (2004).

[7] J. M. Elzerman, R. Hanson, L. H. W. van Beveren, L. M. K. Vandersypen, and L. P. Kouwenhoven, Nature (London) **430**, 431 (2004).

[8] M. V. G. Dutt, L. Childress, L. Jiang, E. Togan, J. Maze, F. Jelezko, A. S. Zibrov, P. R. Hemmer, and M. D. Lukin, Science **316**, 1312 (2007).

[9] L. J. Rogers, K. D. Jahnke, M. H. Metsch, A. Sipahigil, J. M. Binder, T. Teraji, H. Sumiya, J. Isoya, M. D. Lukin, P. Hemmer, and F. Jelezko, Phys. Rev. Lett. **113**, 263602 (2014).

[10] S. O. Valenzuela, W. D. Oliver, D. M. Berns, K. K. Berggren, L. S. Levitov, and T. P. Orlando, Science **314**, 1589 (2006).

[11] M. D. Reed, B. R. Johnson, A. A. Houck, L. DiCarlo, J. M. Chow, D. I. Schuster, L. Frunzio, and R. J. Schoelkopf, Appl. Phys. Lett. **96**, 203110 (2010).

[12] M. Mariantoni, H. Wang, T. Yamamoto, M. Neeley, R. C. Bialczak, Y. Chen, M. Lenander, E. Lucero, A. D. O'Connell, D. Sank, M. Weides, J. Wenner, Y. Yin, J. Zhao, A. N. Korotkov, A. N. Cleland, and J. M. Martinis, Science **334**, 61 (2011).

[13] J. E. Johnson, C. Macklin, D. H. Slichter, R. Vijay, E. B. Weingarten, J. Clarke, and I. Siddiqi, Phys. Rev. Lett. **109**, 050506 (2012).

[14] D. Ristè, J. G. van Leeuwen, H.-S. Ku, K. W. Lehnert, and L. DiCarlo, Phys. Rev. Lett. **109**, 050507 (2012).

[15] D. Ristè, C. C. Bultink, K. W. Lehnert, and L. DiCarlo, Phys. Rev. Lett. **109**, 240502 (2012).

[16] P. Campagne-Ibarcq, E. Flurin, N. Roch, D. Darson, P. Morfin, M. Mirrahimi, M. H. Devoret, F. Mallet, and B. Huard, Phys. Rev. X **3**, 021008 (2013).

[17] Y. Salathé, P. Kurpiers, T. Karg, C. Lang, C. K. Andersen, A. Akin, S. Krinner, C. Eichler, and A. Wallraff, Phys. Rev. Applied **9**, 034011 (2018).

[18] K. Geerlings, Z. Leghtas, I. M. Pop, S. Shankar, L. Frunzio, R. J. Schoelkopf, M. Mirrahimi, and M. H. Devoret, Phys. Rev. Lett. **110**, 120501 (2013).

[19] D. J. Egger, M. Ganzhorn, G. Salis, A. Fuhrer, P. Mueller, and S. Filipp, arXiv:1802.08980.

[20] M. Boissonneault, J. M. Gambetta, and A. Blais, Phys. Rev. A **79**, 013819 (2009).

[21] D. H. Slichter, R. Vijay, S. J. Weber, S. Boutin, M. Boissonneault, J. M. Gambetta, A. Blais, and I. Siddiqi, Phys. Rev. Lett. **109**, 153601 (2012).

[22] D. Sank, Z. Chen, M. Khezri, J. Kelly, R. Barends, B. Campbell, Y. Chen, B. Chiaro, A. Dunsworth, A. Fowler et al., Phys. Rev. Lett. **117**, 190503 (2016).

[23] A. G. Fowler, Phys. Rev. A **88**, 042308 (2013).

[24] M. Grajcar, S. H. W. van der Ploeg, A. Izmalkov, E. Il'ichev, H.-G. Meyer, A. Fedorov, A. Shnirman, and G. Schön, Nat. Phys. **4**, 612 (2008).

[25] D. Basilewitsch, R. Schmidt, D. Sugny, S. Maniscalco, and C. P. Koch, New J. Phys. **19**, 113042 (2017).

[26] K. W. Murch, U. Vool, D. Zhou, S. J. Weber, S. M. Girvin, and I. Siddiqi, Phys. Rev. Lett. **109**, 183602 (2012).

[27] S. P. Premaratne, F. C. Wellstood, and B. S. Palmer, Phys. Rev. A **96**, 043858 (2017).

[28] K. Y. Tan, M. Partanen, R. E. Lake, J. Govenius, S. Masuda, and M. Möttönen, Nat. Commun. **8**, 15189 (2017).

[29] Y. Liu, S. Shankar, N. Ofek, M. Hatridge, A. Narla, K. M. Sliwa, L. Frunzio, R. J. Schoelkopf, and M. H. Devoret, Phys. Rev. X **6**, 011022 (2016).

[30] J. Kelly, R. Barends, B. Campbell, Y. Chen, Z. Chen, B. Chiaro, A. Dunsworth, A. G. Fowler, I.-C. Hoi, E. Jeffrey, A. Megrant, J. Mutus, C. Neill, P. J. J. O'Malley, C. Quintana, P. Roushan, D. Sank, A. Vainsencher, J. Wenner, T. C. White *et al.*, Phys. Rev. Lett. **112**, 240504 (2014).

[31] J. Gambetta, W. A. Braff, A. Wallraff, S. M. Girvin, and R. J. Schoelkopf, Phys. Rev. A **76**, 012325 (2007).

[32] T. Walter, P. Kurpiers, S. Gasparinetti, P. Magnard, A. Potocnik, Y. Salathé, M. Pechal, M. Mondal, M. Oppliger, C. Eichler, and A. Wallraff, Phys. Rev. Applied **7**, 054020 (2017).

[33] M. Pechal, L. Huthmacher, C. Eichler, S. Zeytinoğlu, A. A. Abdumalikov Jr., S. Berger, A. Wallraff, and S. Filipp, Phys. Rev. X **4**, 041010 (2014).

[34] See Supplemental Material at http://link.aps.org/supplemental/10.1103/PhysRevLett.121.060502 for an overview and comparison to prior art, for details about the sample fabrication and parameters, for details about the fit functions for the calibration procedure, for a derivation of the reset operating regimes, for a description of the readout method, for a discussion of the limitations of the reset, and for a description of the master equation simulations.

[35] J. Koch, T. M. Yu, J. Gambetta, A. A. Houck, D. I. Schuster, J. Majer, A. Blais, M. H. Devoret, S. M. Girvin, and R. J. Schoelkopf, Phys. Rev. A **76**, 042319 (2007).

[36] J. A. Schreier, A. A. Houck, J. Koch, D. I. Schuster, B. R. Johnson, J. M. Chow, J. M. Gambetta, J. Majer, L. Frunzio, M. H. Devoret, S. M. Girvin, and R. J. Schoelkopf, Phys. Rev. B **77**, 180502 (2008).

[37] R. Bianchetti, S. Filipp, M. Baur, J. M. Fink, C. Lang, L. Steffen, M. Boissonneault, A. Blais, and A. Wallraff, Phys. Rev. Lett. **105**, 223601 (2010).

[38] B. Yurke, M. L. Roukes, R. Movshovich, and A. N. Pargellis, Appl. Phys. Lett. **69**, 3078 (1996).

[39] C. Eichler and A. Wallraff, Eur. Phys. J. Quantum Technology **1**, 2 (2014).

[40] S. Zeytinoğlu, M. Pechal, S. Berger, A. A. Abdumalikov Jr., A. Wallraff, and S. Filipp, Phys. Rev. A **91**, 043846 (2015).

[41] S. Gasparinetti, S. Berger, A. A. Abdumalikov, M. Pechal, S. Filipp, and A. J. Wallraff, Sci. Adv. **2**, e1501732 (2016).

[42] W. D. Heiss, J. Phys. A **37**, 2455 (2004).

[43] P. Kurpiers, P. Magnard, T. Walter, B. Royer, M. Pechal, J. Heinsoo, Y. Salathé, A. Akin, S. Storz, J.-C. Besse, S. Gasparinetti, A. Blais, and A. Wallraff, Nature (London) **558**, 264 (2018).

[44] J. Heinsoo, C. K. Andersen, S. K. A. Remm, T. Walter, Y. Salathé, S. Gasparinetti, J.-C. Besse, A. Potočnik, C. Eichler, and A. Wallraff, arXiv:1801.07904.

Fast and Unconditional All-Microwave Reset of a Superconducting Qubit
Supplemental Material

S1. PERFORMANCE OF RESET PROTOCOLS FOR SUPERCONDUCTING QUBITS.

We compare experimental implementations of superconducting qubit reset protocols by two performance metrics, the reset rate Γ and the residual excited state population $P_{\mathrm{exc}}^{\mathrm{sat}}$ (Fig. S1). $P_{\mathrm{exc}}^{\mathrm{sat}}$ is obtained at the end of the reset procedure (measurement-based and π-pulse-based reset) or at steady-state (microwave and flux driven reset), corresponding in all cases to the lowest residual excitation reached. For driven reset protocols, Γ is defined as the rate at which the qubit approaches
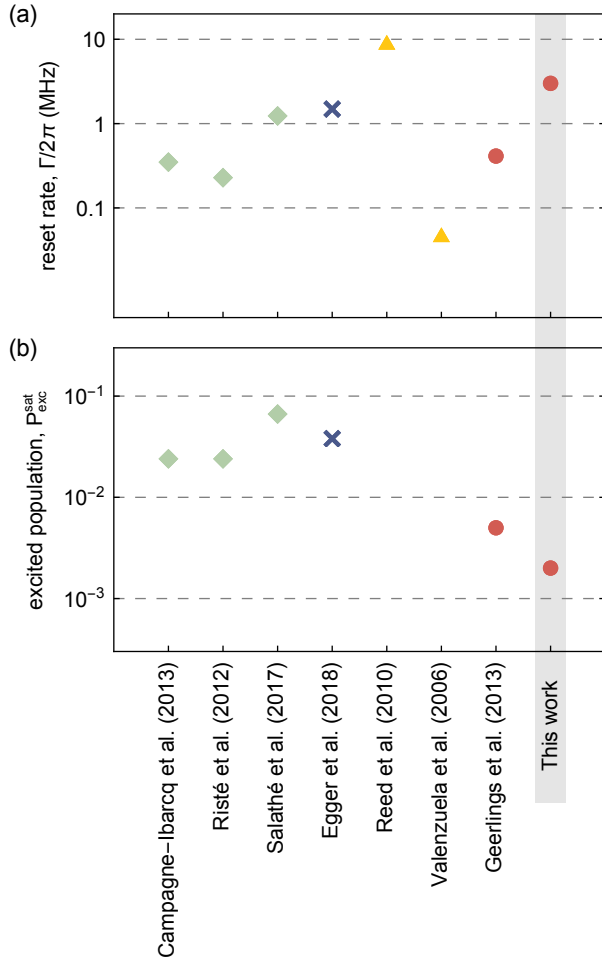
the ground state. For measurement and π-pulse based protocols, Γ satisfies $P_{\mathrm{exc}}^{\mathrm{sat}} = e^{-\Gamma t_p}$, where t_p is the total protocol duration.

In a recent demonstration of a similar protocol, a transmon coupled to a low-Q cavity is reset by applying a sequence of π-pulses on the e-f and f0-g1 transitions [S4]. For a given sample, this alternative scheme leads to a faster reset. As an example, with our sample it is possible to apply e-f and f0-g1 π-pulses in 15 ns and 60 ns, respectively. This would lead to a reset protocol of 75 ns duration plus a photon leakage time $5/\kappa = 90$ ns to empty the cavity. However, unlike our unconditional driven protocol, the reset fidelity is limited by transmon coherence and the π-pulse fidelities. This leads to a reset level $P_{\mathrm{exc}}^{\mathrm{sat}}$ an order of magnitude higher than in the present work.

S2. SAMPLE PARAMETERS

The sample design is similar to the one used in Ref. [S8]. We etch the $\lambda/4$ coplanar waveguide resonators and feed-lines from a thin niobium film on a sapphire substrate using standard photolithography techniques. The transmon capacitor pads and Josephson junctions are fabricated using electron-beam lithography and shadow evaporation of aluminum. The parameters of the readout circuit (green elements in Fig.1a) and reset circuit (blue elements in Fig.1a) are obtained from fits to the

FIG. S1. Experimentally achieved reset rates Γ (a) and residual excited state populations $P_{\mathrm{exc}}^{\mathrm{sat}}$ (b) of selected implementations of superconducting qubit reset protocols based on: qubit measurement and feedback control (green squares) [S1–S3], sequential π-pulses to a dissipative state (blue cross) [S4], qubit frequency tuning via flux pulses (yellow triangles) [S5, S6] and all-microwave drive induced dissipation (red circles) [S7].

$\omega_{\mathrm{ge}}/2\pi$	6.343 GHz		
$\alpha/2\pi$	-265 MHz		
n_{th}	17 %		
T_1^{ge}	5.5 μs	T_1^{ef}	2.1 μs
T_2^{ge}	7.6 μs	T_2^{ef}	4.2 μs
$T_2^{*\mathrm{ge}}$	3.5 μs	$T_2^{*\mathrm{ef}}$	2.0 μs
$\chi_m/2\pi$	-5.8 MHz	$\chi_r/2\pi$	-6.3 MHz
$g_m/2\pi$	210 MHz	$g_r/2\pi$	335 MHz
$\omega_m/2\pi$	4.787 GHz	$\omega_r/2\pi$	8.400 GHz
$\omega_{PFm}/2\pi$	4.778 GHz	$\omega_{PFr}/2\pi$	8.443 GHz
Q_{PFm}	91	Q_{PFr}	60
$J_m/2\pi$	13.6 MHz	$J_r/2\pi$	20.9 MHz
$\kappa_m/2\pi$	12.6 MHz	$\kappa/2\pi$	9.0 MHz

TABLE I. Sample parameters: From time resolved Ramsey measurements we extract the ge transition frequency $\omega_{\mathrm{ge}}/2\pi$, and the anharmonicity $\alpha/2\pi$. From resonator transmission spectroscopy we obtain the frequencies, quality factors and couplings of the measurement (m) and reset (r) resonators: Purcell filter frequency $\omega_{\mathrm{PF_{m,r}}}/2\pi$, resonator frequency $\omega_{\mathrm{m,r}}/2\pi$, quality factor of the Purcell filter $Q_{\mathrm{PF_{m,r}}}$ and the coupling rate of the resonator to Purcell filter $J_{\mathrm{m,r}}/2\pi$. We obtain the dispersive shifts $\chi_{\mathrm{m,r}}/2\pi$ by performing resonator spectroscopy with the qutrit initially prepared in $|g\rangle$, $|e\rangle$ and $|f\rangle$. The coherence times of the qutrit are extracted from time resolved measurements.

transmission spectrum of the respective Purcell filter using the technique and model discussed in Ref. [S8] and are listed in Table I. We extract the coupling strength of the transmon to both circuits using the same fitting procedure while preparing the transmon in its ground or excited state. The transition frequency $\omega_{\text{ge}}/2\pi$, the anharmonicity α and the coherence times $T_{2\text{ge}}^{\text{R}}$, $T_{2\text{ef}}^{\text{R}}$ are measured using Ramsey-type measurements. The energy decay time T_1^{ge} (T_1^{ef}) is extracted from an exponential fit to the measured time dependence of the populations when preparing the qubit in ether $|e\rangle$ or $|f\rangle$. The population n_{th} of state $|e\rangle$ in thermal equilibrium is extracted with the Rabi population measurement (RPM) method introduced in Ref. [S7]. We used a miniature superconducting coil to thread flux through the SQUID of the transmon to tune $\omega_{\text{ge}}/2\pi$.

S3. RABI RATE EXTRACTION

In the fourth calibration step discussed in the main text, to measure the linear relation between the drive rate $\tilde{g}$ and drive amplitude V_{f0g1}, we perform Rabi oscillation measurements (Fig. 2d and f). To analyze these oscillations, we use a two-level model with loss described by the non-Hermitian Hamiltonian

$$H_{\text{f0g1}} = \begin{bmatrix} i\gamma/2 & \tilde{g} \\ \tilde{g}^* & i\kappa/2 \end{bmatrix}, \quad \text{(S1)}$$

which acts on states $|f, 0\rangle$ and $|g, 1\rangle$, analyzed in a rotating frame. The non-Hermitian terms $i\kappa/2$ and $i\gamma/2$ account for photon emission and transmon decay from $|f\rangle$ to $|e\rangle$, which bring the system to the dark states $|g, 0\rangle$ and $|e, 0\rangle$, respectively. Based on this model we derive an analytical expression for the $|f\rangle$ state population as a function of time

$$P_{\text{f}}(t) = e^{-\frac{(\kappa+\gamma)}{2}t} \left| \cosh\left(\frac{\Omega t}{2}\right) + \frac{\kappa-\gamma}{2\Omega} \sinh\left(\frac{\Omega t}{2}\right) \right|^2, \quad \text{(S2)}$$

where $\Omega = \sqrt{-(2\tilde{g})^2 + (\kappa-\gamma)^2/4}$ is real positive or imaginary depending on the drive rate $\tilde{g}$. Using $P_{\text{f}}(t)$ we obtain the fit function

$$f_{\tilde{g}}(t) = \lambda P_{\text{f}}(t - t_0) + \mu, \quad \text{(S3)}$$

where the parameters λ and μ account for potential state preparation and measurement (SPAM) errors and the parameter t_0 accounts for the fact that the gaussian rising and falling edges of the flat top f0-g1 pulse drive the f0-g1 transition for a finite time. For each drive amplitude V_{f0g1}, we obtain Rabi oscillation data which we fit with Eq. (S3). To reduce the number of free parameters, we fit all data sets simultaneously and constrain λ, μ, t_0 and κ to be the the same for all sets as these parameters are expected to be independent of V_{f0g1}.

In the second calibration step discussed in the main text, we measure the linear dependence of the drive rate

Ω_{ef} on the drive amplitude V_{ef}, by performing Rabi oscillation measurements (Fig. 2b and d). We fit the time-dependence of the population P_{e} with the function

$$f_{\Omega_{\text{ef}}}(t) = \frac{1}{2} e^{-\gamma_a t^*} \left(1 - e^{-\gamma_b t^*} \cos\left(\frac{\Omega_{\text{ef}} t^*}{2}\right) \right), \quad \text{(S4)}$$

where $t^* = t - t_0$ offsets the time t by t_0 to account for the fact that the rising and falling edges of the e-f pulse drive the e-f transition for a finite time. The fit parameters γ_a and γ_b account for transmon relaxation to $|g\rangle$ and decoherence in the $\{|e\rangle, |f\rangle\}$ subspace, respectively. We verified numerically that Eq. (S4) is a good approximation of the time dependence of P_{e} during e-f Rabi oscillations and that it yields an unbiased estimate of Ω_{ef}, by comparing it to the result of a master equation simulation. Similarly to the f0-g1 Rabi rate calibration, we simultaneously fit the Rabi oscillation data sets obtained for all probed V_{ef}, constraining the fit parameter t_0, γ_a and γ_b to be the the same for all sets.

S4. RESET OPERATING REGIMES

The discussion about the reset operating regimes is based on Eq. (2) in the main text. To derive this equation, we start with the expression for the population

$$P_{\text{s}|\text{s}_0}^{\text{H}}(t) = \left| \langle s | e^{-iHt} | s_0 \rangle \right|^2,$$

of state $|s\rangle \in \{|e, 0\rangle, |f, 0\rangle, |g, 1\rangle\}$, where s_0 is the initial state. We introduce the diagonalization matrix

$$T = \sum_k |\lambda_k\rangle \langle k|,$$

where $|\lambda_k\rangle$ are the eigenvectors of H and the vectors $|k\rangle$ form an orthonormal basis in which $D = T^{-1} \cdot H \cdot T$ is diagonal. Note that, since H is non-Hermitian, its eigenvectors $|\lambda_k\rangle$ are not orthogonal and T is not unitary. We then obtain

$$P_{\text{s}|\text{s}_0}^{\text{H}}(t) = \left| \langle s | T e^{-iDt} T^{-1} | s_0 \rangle \right|^2$$

$$= \left| \sum_{jklm} \langle s | T_{jk} | j \rangle \langle k | e^{-iDt} T_{lm}^{-1} | l \rangle \langle m | s_0 \rangle \right|^2$$

$$= \left| \sum_k \langle s | \left(\sum_{jm} T_{jk} T_{km}^{-1} | j \rangle \langle m | \right) | s_0 \rangle e^{-i\lambda_k t} \right|^2.$$

We recover Eq. (2) by defining

$$\hat{A}_k = \sum_{jm} T_{jk} T_{km}^{-1} | j \rangle \langle m |.$$

As discussed in the main text, we can define operating regimes of the reset by studying the eigenvalues λ_k of Hamiltonian (1). We set $\delta_{\text{ef}} = \delta_{\text{f0g1}} = 0$, both to simplify

the analysis and to ensure that the full three-level transmon is reset. To reduce the notations, we tackle an equivalent problem and solve for the eigenvalues $\Lambda_k = i2\lambda_k/\kappa$ of the renormalized Hamiltonian

$$\tilde{H} = \begin{bmatrix} 0 & \sqrt{\Omega} & 0 \\ -\sqrt{\Omega} & 0 & \sqrt{G} \\ 0 & -\sqrt{G} & -1 \end{bmatrix}, \quad (S5)$$

where the dimensionless drive powers $\Omega = (2\Omega_{\text{ef}}/\kappa)^2$ and $G = (2\tilde{g}/\kappa)^2$ are real and positive. Hamiltonian (S5) has the characteristic polynomial

$$P_{\tilde{H}}(X) = X^3 + X^2 + (G+\Omega)X + \Omega, \quad (S6)$$

whose roots are the eigenvalues Λ_k. The discriminants of this cubic equation are

$$\Delta_0 = 1 - 3(G+\Omega), \quad (S7)$$
$$\Delta_1 = 2 - 9(G - 2\Omega). \quad (S8)$$

Note that Δ_0 is a linear function of $G+\Omega$, so $(-\Delta_0)$ indicates the amount of total drive power. Conversely, Δ_1 indicates the level of asymmetry between the power of the two drives. Defining the sub-roots

$$C^\pm = \sqrt[3]{\frac{\Delta_1 \pm \sqrt{\Delta_1^2 - 4\Delta_0^3}}{2}}, \quad (S9)$$

we find the expression for the eigenvalues

$$\Lambda_k = -\frac{1}{3}\left(1 + \xi^k C^+ + \xi^{-k} C^-\right), \quad (S10)$$

where $k \in \{-1, 0, 1\}$, and $\xi^k = \exp[i2\pi k/3]$ are the cubic roots of unity. A consequence of Eq. (S10) is that the reset rate is bounded by $\Gamma/\kappa \equiv \min|\text{Re}(\Lambda_k)| \leq 1/3$. We can distinguish three cases based on the sign of $\Delta_1^2 - 4\Delta_0^3$.

Under-damped regime: $\Delta_1^2 > 4\Delta_0^3$. In this case, the sub-roots C^+ and C^- are real and distinct from each other. Therefore, the eigenvalues Λ_k are complex, with a non-zero imaginary part: the populations display oscillations during the reset. Depending on the sign of Δ_1, we have

$$\Gamma/\kappa = \begin{cases} \frac{1}{3}\left[1 - \frac{1}{2}(C^+ + C^-)\right] < \frac{1}{3} & \text{, if } \Delta_1 > 0 \\ \frac{1}{3}\left[1 + (C^+ + C^-)\right] < \frac{1}{3} & \text{, if } \Delta_1 < 0 \\ \frac{1}{3} & \text{, if } \Delta_1 = 0. \end{cases} \quad (S11)$$

The reset rate is thus maximized ($\Gamma = \kappa/3$) only when the drives are strong enough ($\Delta_0 \leq 0$) and well balanced ($\Delta_1 = 0$). The conditions $\Delta_0 \leq 0$ and $\Delta_1 = 0$ define the optimal branch (solid red line in Fig. 3a).

Over-damped regime: $\Delta_1^2 < 4\Delta_0^3$. In this low power regime (Δ_0 has to be positive), C^+ and C^- are complex conjugates of each other. As a result, all eigenvalues Λ_k are purely real and the qutrit populations show no oscillatory features during the reset. In this regime, the reset rate can be expressed as

$$\Gamma/\kappa = \frac{1}{3}\left[1 - \sqrt{\Delta_0}\left(\cos\frac{\theta}{3} + \sqrt{3}\sin\frac{\theta}{3}\right)\right],$$

where $\theta = \arccos(\Delta_1/2\Delta_0^{3/2})$ is the argument of $(C^+)^3$, and ranges from 0 to π. Because $\Delta_0 > 0$, we have the strict inequality $\Gamma < \kappa/3$, which means that the optimal branch does not cross the over-damped region.

Critical-damping: $\Delta_1^2 = 4\Delta_0^3$. When this equality holds, we have $C^+ = C^- = \sqrt[3]{\Delta_1/2} = \sqrt{\Delta_0}$, and the eigenvalues are real. We parametrize the critical damping equality by introducing the variable $\beta = \sqrt[3]{\Delta_1/2}$. We then have $\Delta_0 = \beta^2$ and $C^\pm = \beta$, which leads to

$$\Gamma/\kappa = \begin{cases} \frac{1}{3}(1 - \beta) & \text{, if } \beta \geq 0 \\ \frac{1}{3}(1 + 2\beta) & \text{, otherwise.} \end{cases} \quad (S12)$$

Inverting Eqs. (S7) and (S8) we obtain a parametrization of the critical damping boundary region

$$G(\beta) = \frac{8}{27}(1 - \frac{3}{4}\beta^2 - \frac{1}{4}\beta^3),$$
$$\Omega(\beta) = \frac{1}{27}(1 - 3\beta^2 + 2\beta^3),$$

where β ranges from $-1/2$ to 1, to keep Γ, G and Ω positive.

For $\beta = 0$, we have $\Gamma = \kappa/3$. This point is an exceptional point, where all eigenvalues are identical (Eq. (S10) with $C^\pm = 0$) and the eigenvectors coalesce [S9]. This point ($G = 8/27$ and $\Omega = 1/27$, or equivalently, $\tilde{g} = \tilde{g}_{\text{ep}} = \sqrt{2/27}\kappa$ and $\Omega_{\text{ef}} = \Omega_{\text{ef,ep}} = \sqrt{1/108}\kappa$) is the only one that maximizes Γ without displaying oscillatory features of the populations.

For a given value of G, there is a unique Ω^{opt} that maximizes the reset rate to $\Gamma_{\text{max}}(G)$. For $G \geq 8/27$, according to Eq. (S11), the reset rate is maximized by chosing Ω such that $\Delta_1 = 0$. Using Eq. (S8), we find that $\Omega_{\text{opt}}(G) = G/2 - 1/9$. The parameters are then on the optimal branch and $\Gamma_{\text{max}}(G) = \kappa/3$. For $G < 8/27$, the reset rate is maximized by chosing Ω such that $\Delta_1^2 = 4\Delta_0^3$ (critical damping) and $\Delta_1 > 0$ (upper branch). This can be proven by showing that $\partial_\Omega\Gamma \geq 0$ in the over-damped region, and that $\partial_\Omega\Gamma$ and Δ_1 have opposite signs in the under-damped region. Using these results, we obtain

$$\Gamma_{\text{max}}(G) = \frac{2}{3}\left[1 - \cos\left(\frac{1}{3}\arccos\left(1 - \frac{27G}{4}\right)\right)\right].$$

The derivative of Γ_{max} diverges as $G \to 8/27$ from the left side (Fig. 3b). If one cannot drive the f0-g1 transition with enough power to get $G > 8/27$, or equivalently $\tilde{g} > \sqrt{2/27}\kappa$, Γ_{max} is abruptly reduced. To obtain a fast reset, one should therefore target a value of κ that is as high as possible within the limit that $\kappa < \tilde{g}_{\text{max}}\sqrt{27/2} \simeq 3.67\tilde{g}_{\text{max}}$, where $\tilde{g}_{\text{max}}$ is the maximum f0-g1 drive rate experimentally achievable, without driving unwanted transitions [S10]. This ensures that the maximum reset rate $\Gamma = \kappa/3$ is high and always attainable.

	$|g\rangle$	$|e\rangle$	$|f\rangle$
g	98.2	2.5	2.4
e	0.9	95.7	4.6
f	0.9	1.8	93.0

TABLE II. Reference assignment probability matrix of identifying prepared states (columns) as the measured states (rows). The diagonal elements show correct identification, the off-diagonal elements misidentifications.

reference sets of 40000 single-shot traces obtained with the transmon initialized in states $|g\rangle$, $|e\rangle$ or $|f\rangle$. State initialization is performed using a pre-selection readout pulse that heralds the transmon in its ground state (details discussed later in this section) followed by control π-pulses to prepare states $|e\rangle$ and $|f\rangle$ (Fig. S2b). We integrate each reference single-shot trace with weight functions w_1 and w_2, to calculate the integrated quadratures $u = \int_0^{t_{\rm m}} S(t)w_1(t)dt$ and $v = \int_0^{t_{\rm m}} S(t)w_2(t)dt$, in post-processing. We choose w_1 and w_2 such that they maximize the distinguishability between the three qutrit states. For each prepared state $|p\rangle$, the set of integrated traces $\vec{x} = (u, v)$ forms three clusters in the u-v plane (Fig. S2c) following a trimodal Gaussian distribution of mixture density

$$f_{\rm p}(\vec{x}) = \sum_s \frac{A_{\rm s,p}}{2\pi\sqrt{|\Sigma|}} e^{-\frac{1}{2}(\vec{x}-\mu_s)^\top \cdot \Sigma^{-1} \cdot (\vec{x}-\mu_s)}. \quad (S13)$$

We extract the parameters $A_{\rm s,p}$, Σ and μ_s with maximum likelihood estimation. Based on these parameters, we define regions in the u-v plane used to assign the result of the readout trace: if an integrated trace $\vec{x}_i$ is in the region labeled m, we assign it state m (Fig. S2c). By counting the number of traces assigned the value m when the qutrit was prepared in state $|s\rangle$, we estimate the elements $R_{\rm m,s} = p(m|\,|s\rangle)$ of the reference assignment probability matrix R (see Table II).

To extract the qutrit state populations $P = (P_{\rm g}, P_{\rm e}, P_{\rm f})$ after a reset of duration $t_{\rm r}$, we also repeat the scheme illustrated in Fig. S2a 40000 times, and record single-shot traces for each run. As for the reference sets, the assignment probability $M_{\rm m}$ is estimated by counting the number of traces assigned the value m and follows

$$M_{\rm m} = p(m|P) = \sum_s R_{\rm m,s} \cdot P_{\rm s}, \quad (S14)$$

which can be expressed as $M = R \cdot P$. A simple approach to estimate the population P of the qutrit is to set $P = M$. This approach is, however, sensitive to assignment errors due to readout imperfections: $P = M$ holds true only if $R_{\rm m,s} = \delta_{\rm m,s}$. To account for readout errors, we invert Eq. (S14) and set $P = R^{-1} \cdot M$. However, this procedure relies on the accurate characterization of R, which is sensitive to errors in state-preparation for the reference trace sets. The qutrit therefore needs to be initialized in $|g\rangle$ before applying the reference readout tone, with a residual excitation that can be
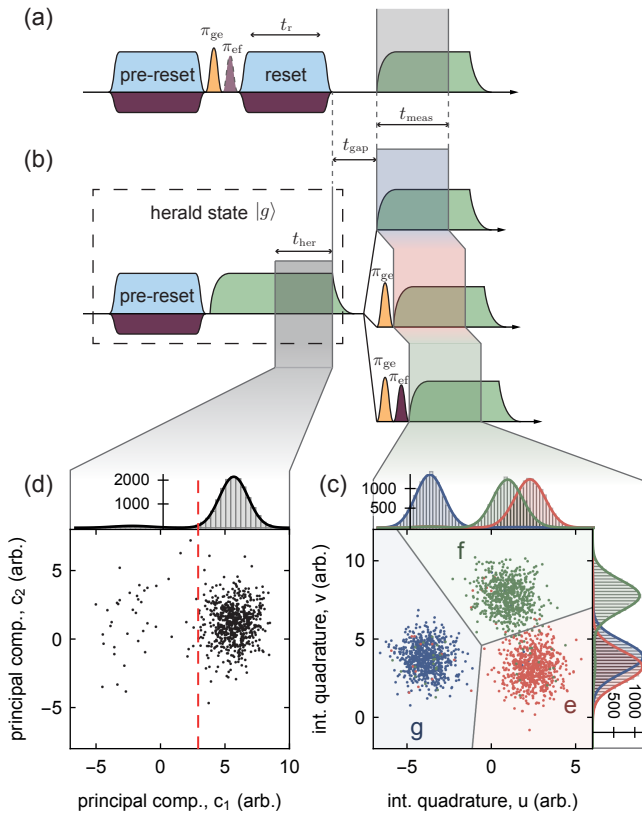
FIG. S2. (a) Schematic of the pulse scheme used to test the unconditional reset protocol. (b) Schematic of the pulse scheme used to record reference single-shot counts. (c) Subset of 500 reference traces displayed in the u-v plane, when the qutrit is prepared in state $|g\rangle$ (blue dots), $|e\rangle$ (red dots) or $|f\rangle$ (green dots). The assignment regions labeled g, e and f are shaded in blue, red and green, respectively, and are separated by a gray line at their boundaries. (d) Sub-sample of 1000 traces acquired during the pre-selection pulse, projected in the principal component plane c_1-c_2. Here c_1 and c_2 are the two first principal components of the set of traces. The red dashed line indicates the threshold for selection/rejection of traces. The plots on the top or right axes of (c) and (d) show histogram counts of the traces. The solid lines in these plots correspond to the density of the marginal probability distributions of the traces, scaled to match the histograms.

S5. SINGLE-SHOT READOUT

To study the reset dynamics (Fig. 4), we pre-reset the transmon with an unconditional reset, and prepare it in state $|e, 0\rangle$ or $|f, 0\rangle$ with a sequence of π-pulses (Fig. S2a). Next, we apply the reset pulses for a duration $t_{\rm r}$ and apply a microwave tone at the readout resonator to readout the transmon. We record the I and Q quadratures of the readout signal for a duration of $t_{\rm m} = 120\,{\rm ns}$ starting at the rising edge of the readout tone. We refer to each recorded readout signal as a single-shot trace S.

To define an assignment rule which discriminates the transmon state based on a single-shot trace, we collect

bounded, and that is ideally smaller than that of the unconditional reset protocol presented in this manuscript. As mentioned earlier in this section, to do so, we pre-reset the transmon with our protocol, then herald the ground state of the transmon with a pre-selection readout pulse (Fig. S2b). We record single-shot traces during the last $72\,\mathrm{ns}$ of the pre-selection pulse t_{her}. The pre-selection traces form two clusters, corresponding to ground and excited traces, that are maximally separated along their first principal component axis (Fig. S2c). We model the distribution of the first principal component c_1 of the traces with a bimodal Gaussian distribution and extract its parameters with maximum-likelihood estimation. Based on this model, we calculate a threshold value c_{thr} such that $p(c_1 > c_{\mathrm{thr}}|\mathrm{exc}) = 10^{-5}$. Selecting only traces with $c_1 > c_{\mathrm{thr}}$ heralds the ground state of the transmon. On the set of selected traces, the residual excitation of the transmon at the rising edge of the reference readout tone is therefore dominated by transmon thermalization, which occurs at rate $k_\uparrow/2\pi = 5\,\mathrm{kHz}$ in our sample. We use the same waiting time t_{gap} between initialization and readout to characterize the unconditional reset dynamics (Fig. S2a) and the reference trace set (Fig. S2b). As a result, thermalization occuring during this time can be seen as a source of readout error, which is compensated for. State preparation errors are then mostly explained by transmon thermalization occuring during the pre-selection, which we can bound by $k_\uparrow t_{\mathrm{her}} \simeq 0.25\%$.

In conclusion, the corrected single-shot readout method we developed suffers from state preparation error resulting in a systematic under-estimation of the extracted populations, bounded by 0.25%. This residual error is small compared to the populations extracted during the unconditional reset for most measured points (Fig. 4c); this readout method is therefore suitable for the analysis presented here.

S6. LIMITATIONS OF THE RESET PROTOCOL

The steady-state excited population $P_{\mathrm{exc}}^{\mathrm{sat}}$ which can be reached with the unconditional reset is constrained by three effects: transmon rethermalization, finite temperature of the reset resonator, and off-resonant driving of the g-e transition with the e-f drive. These constraints are quantitatively modelled in our master equation simulation, but they can also be discussed qualitatively to understand their effects on the performance.

The effective temperatures of superconducting qubits are typically higher than the base temperature of the dilution refrigerator T_{BT}, which implies that the thermal excitation rate $k_\uparrow$ of the qubit is higher than expected from T_{BT} [S11]. At equilibrium, thermalization competes against decay and the qubit has an equilibrium excited population $n_{\mathrm{th}} \simeq k_\uparrow T_1$ (in the limit where $n_{\mathrm{th}} \ll 1$). Similarly, for the unconditional reset protocol, the competition between thermalization and reset rate yields the

steady-state excitation population $P_{\mathrm{ecx}}^{\mathrm{sat}} \sim k_\uparrow/\Gamma$. We model thermal excitations as quantum jumps to derive an analytical expression for $P_{\mathrm{ecx}}^{\mathrm{sat}}$. In steady state, the probability of a transmon rethermalization event (jump from $|g\rangle$ to $|e\rangle$) occurring between times $-t$ and $-t + dt$ is $(1 - P_{\mathrm{ecx}}^{\mathrm{sat}})k_\uparrow dt \simeq k_\uparrow d\tau$. If such an event happens at time $-t$, the excited population a time 0 is $[P_{\mathrm{e|e}}^{\mathrm{H}} + P_{\mathrm{f|e}}^{\mathrm{H}}](t)$ as defined from Eq. (2) (main text). Integrating over all possible time windows for a rethermalization jump to occur, we obtain $P_{\mathrm{ecx}}^{\mathrm{sat}} = \int_0^{+\infty}[P_{\mathrm{e|e}}^{\mathrm{H}} + P_{\mathrm{f|e}}^{\mathrm{H}}](t)k_\uparrow dt = k_\uparrow \tau$, which tends towards $k_\uparrow/\Gamma$ for large drive rates. Using this method, we calculate $P_{\mathrm{ecx}}^{\mathrm{sat}} = 0.26\%$, 0.46% and 0.34% for configuration A, B and C, respectively. The close agreement of the calculated $P_{\mathrm{ecx}}^{\mathrm{sat}}$ with its measured and simulated values for all parameter configurations further supports our interpretation that transmon rethermalization is the dominant factor limiting the final population after reset.

In the level diagram of Fig. 1b, the black arrow labelled κ, connecting $|g,1\rangle$ to $|g,0\rangle$ represents the decay of the reset resonator. A finite temperature T_{rr} of the reset resonator can be accounted for by a transition in the opposite direction with rate $\kappa \cdot \exp[-\hbar\omega_{\mathrm{r}}/k_{\mathrm{b}}T_{\mathrm{rr}}]$. If the unconditional reset is dominated by this rate, the entropy of the transmon and of the resonator equalize and the temperature of the transmon reaches $T_{\mathrm{rr}}\omega_{\mathrm{ge}}/\omega_{\mathrm{r}}$ in steady-state.

Driving the e-f transition during unconditional reset broadens also the g-e transition. The e-f drive, being detuned from the g-e transition by approximately the anharmonicity α of the transmon, also drives the g-e transition which leads to e-f drive induced thermalization. A trade-off between speed and reset fidelity has to be made when this effect is limiting.

The parameters we chose to optimize the reset are not the cause for the relatively large rethermalization rate $k_\uparrow/2\pi \simeq 5\,\mathrm{kHz}$ measured in our sample ($n_{\mathrm{th}} = 17\,\%$ and $T_1 = 5.5\,\mu s$). Indeed, Purcell decay through both resonators would allow for relaxation times up to $T_1^{\mathrm{Purcell}} = 370\,\mu s$ [S12]. In addition, we observed thermal excitation levels as low as $n_{\mathrm{th}} = 0.3\,\%$ in a sample with similar design and parameters in previous work [S8]. Therefore, with improved fabrication processes we expect to be able to decrease the rethermalization rate down to $k_\uparrow/2\pi \simeq 0.2\,\mathrm{kHz}$ ($n_{\mathrm{th}} < 5\,\%$ and $T_1 \sim 30\,\mu s$). With such a rate, transmon rethermalization would not limit the reset any more and we expect to reach saturation levels as low as $P_{\mathrm{ecx}}^{\mathrm{sat}} = 2 \times 10^{-4}$ with the current sample parameters.

S7. MASTER EQUATION SIMULATION

To model the transmon qutrit reset process numerically, we start with the Hamiltonian of a transmon dispersively coupled to a high bandwidth resonator. We add the two drive-induced couplings required for the unconditional reset protocol, i.e. a Rabi drive between the $|e\rangle$, $|f\rangle$

states of the transmon combined with an effective coupling $\tilde{g}$ between the $|f,0\rangle, |g,1\rangle$ states of the transmon-resonator system [S10, S13]. We represent the transmon as an anharmonic oscillator with annihilation and creation operators $\hat{b}$, $\hat{b}^\dagger$ [S14] which we truncate at the second excited state $|f\rangle$ and denote the annihilation and creation operators of the reset resonator $\hat{a}$ and $\hat{a}^\dagger$, respectively. In a frame rotating at ω_r for the resonator and $\omega_{ge} + \alpha/2$ for the transmon, the transmon-resonator system is described by the Hamiltonian

$$
\begin{aligned}
\hat{H} = & -\frac{\alpha}{2}\hat{b}^\dagger \hat{b} + \frac{\alpha}{2}\hat{b}^\dagger \hat{b}^\dagger \hat{b}\hat{b} + 2\chi_r \hat{a}^\dagger \hat{a}\hat{b}^\dagger \hat{b} \\
& + \frac{\tilde{g}}{\sqrt{2}}(\hat{b}^\dagger \hat{b}^\dagger \hat{a} + \hat{a}^\dagger \hat{b}\hat{b}) + \frac{\Omega_{\text{ef}}}{\sqrt{2}}(\hat{b}\,e^{i\alpha t/2} + \hat{b}^\dagger e^{-i\alpha t/2}),
\end{aligned}
\tag{S15}
$$

where α is the transmon anharmonicity, χ_r the dispersive coupling strength between the transmon and the resonator, and Ω_{ef} is the Rabi rate between the $|e\rangle, |f\rangle$ states of the transmon. The readout resonator is omitted from the Hamiltonian since it does not affect the reset process and the induced static Lamb shifts are implicitly included in the parameters.

Numerical results are obtained by initializing the sytem in the $|e,0\rangle$ state and integrating the master equation

$$
\begin{aligned}
\dot{\rho} = & -i[\hat{H}, \rho] \\
& + \kappa \mathcal{D}[\hat{a}]\rho + \kappa_{\text{int}}\mathcal{D}[\hat{a}]\rho \\
& + \gamma_{1ge}(1 + n_{\text{th}})\mathcal{D}\left[|g\rangle\langle e|\right]\rho + \gamma_{1ge}n_{\text{th}}\mathcal{D}\left[|e\rangle\langle g|\right]\rho \\
& + \gamma_{1ef}(1 + n_{\text{th}})\mathcal{D}\left[|e\rangle\langle f|\right]\rho + \gamma_{1ef}n_{\text{th}}\mathcal{D}\left[|f\rangle\langle e|\right]\rho \\
& + \frac{\gamma_{\phi\text{ge}}}{2}\mathcal{D}\left[|e\rangle\langle e| - |g\rangle\langle g|\right]\rho \\
& + \frac{\gamma_{\phi\text{ef}}}{2}\mathcal{D}\left[|f\rangle\langle f| - |e\rangle\langle e|\right]\rho,
\end{aligned}
\tag{S16}
$$

where $\mathcal{D}[\hat{O}]\bullet = \hat{O}\bullet\hat{O}^\dagger - \{\hat{O}^\dagger\hat{O}, \bullet\}/2$ denotes the dissipation super-operator, κ_{int} the internal decay rate of the resonator, $\gamma_{1nm} = 1/T_{1nm}$ the decay rates of the transmon between the $|n\rangle, |m\rangle$ states, $\gamma_{\phi nm} = 1/2T_1^{\text{nm}} - 1/T_2^{\text{nm}}$ the dephasing rates between the $|n\rangle, |m\rangle$ states of the transmon and n_{th} the thermal population of the transmon qubit in steady state.

[S1] D. Ristè, J. G. van Leeuwen, H.-S. Ku, K. W. Lehnert, and L. DiCarlo, Phys. Rev. Lett. **109**, 050507 (2012).

[S2] P. Campagne-Ibarcq, E. Flurin, N. Roch, D. Darson, P. Morfin, M. Mirrahimi, M. H. Devoret, F. Mallet, and B. Huard, Phys. Rev. X **3**, 021008 (2013).

[S3] Y. Salathé, P. Kurpiers, T. Karg, C. Lang, C. K. Andersen, A. Akin, S. Krinner, C. Eichler, and A. Wallraff, Phys. Rev. Applied **9**, 034011 (2018).

[S4] D. J. Egger, M. Ganzhorn, G. Salis, A. Fuhrer, P. Mueller, and S. Filipp, ArXiv:1802.08980 (2018), arXiv:1802.08980 [quant-ph].

[S5] S. O. Valenzuela, W. D. Oliver, D. M. Berns, K. K. Berggren, L. S. Levitov, and T. P. Orlando, Science **314**, 1589 (2006), http://www.sciencemag.org/content/314/5805/1589.full.pdf.

[S6] M. D. Reed, B. R. Johnson, A. A. Houck, L. DiCarlo, J. M. Chow, D. I. Schuster, L. Frunzio, and R. J. Schoelkopf, Appl. Phys. Lett. **96**, 203110 (2010).

[S7] K. Geerlings, Z. Leghtas, I. M. Pop, S. Shankar, L. Frunzio, R. J. Schoelkopf, M. Mirrahimi, and M. H. Devoret, Phys. Rev. Lett. **110**, 120501 (2013).

[S8] T. Walter, P. Kurpiers, S. Gasparinetti, P. Magnard, A. Potocnik, Y. Salathé, M. Pechal, M. Mondal, M. Oppliger, C. Eichler, and A. Wallraff, Phys. Rev. Applied **7**, 054020 (2017).

[S9] W. D. Heiss, Journal of Physics A: Mathematical and General **37**, 2455 (2004).

[S10] S. Zeytinoğlu, M. Pechal, S. Berger, A. A. Abdumalikov Jr., A. Wallraff, and S. Filipp, Phys. Rev. A **91**, 043846 (2015).

[S11] X. Y. Jin, A. Kamal, A. P. Sears, T. Gudmundsen, D. Hover, J. Miloshi, R. Slattery, F. Yan, J. Yoder, T. P. Orlando, S. Gustavsson, and W. D. Oliver, Phys. Rev. Lett. **114**, 240501 (2015).

[S12] E. A. Sete, J. M. Martinis, and A. N. Korotkov, Phys. Rev. A **92**, 012325 (2015).

[S13] M. Pechal, L. Huthmacher, C. Eichler, S. Zeytinoğlu, A. A. Abdumalikov Jr., S. Berger, A. Wallraff, and S. Filipp, Phys. Rev. X **4**, 041010 (2014).

[S14] J. Koch, T. M. Yu, J. Gambetta, A. A. Houck, D. I. Schuster, J. Majer, A. Blais, M. H. Devoret, S. M. Girvin, and R. J. Schoelkopf, Phys. Rev. A **76**, 042319 (2007).